Journal of Alloys and Compounds 510 (2012) 97–106

Contents lists available at SciVerse ScienceDirect

Journal of Alloys and Compounds

journal homepage: www.elsevier.com/locate/jallcom

# Compositional optimization of vanadium-free hypo-stoichiometric $AB_2$ metal hydride alloy for Ni/MH battery application

K. Young*, T. Ouchi, J. Koch, M.A. Fetcenko

*Energy Conversion Devices Inc./Ovonic Battery Company, 2983 Waterview Drive, Rochester Hills, MI 48309, USA*

ARTICLE INFO

*Article history:*
Received 13 July 2011
Received in revised form 26 August 2011
Accepted 29 August 2011
Available online 6 September 2011

*Keywords:*
Hydrogen absorbing materials
Transition metal alloys
Metal hydride electrode
Electrochemical reactions

ABSTRACT

In an effort to reduce raw material cost and improve the charge retention characteristic of nickel metal hydride batteries, the Ti, Zr, and Ni-contents in vanadium-free $AB_2$ metal hydride alloys were optimized according to their capacity, charge retention, activation, high-rate capability, low-temperature performance, and cycle stability. A multi-component hypo-stoichiometric $AB_2$ alloy with a composition of $Ti_{10}Zr_{27}Cr_8Mn_{15}Co_5Ni_{35}$ was identified and compared to vanadium-containing $AB_2$ metal hydride alloys. Vanadium-free alloys provided better charge retention performance but with a trade-off in cycle life. The gaseous and electrochemical storage properties were correlated to both the average composition and the stoichiometry of the main $AB_2$ phases.

## 1. Introduction

Laves phases based $AB_2$ metal hydride (MH) alloys are important candidates as negative electrode active materials in nickel–metal hydride (Ni/MH) batteries for applications such as small portable electronic devices, hybrid and electrical vehicles, and stationary energy storages [1–4]. Other candidates include LaMgNiCo [5–8], Ti–V based BCC [9], and MmMgNiAl alloys [10]. In the large-scale stationary applications of solar and wind farm storage, round-trip energy storage efficiency has become one of the key factors to be considered when choosing the battery chemistry. Commercial-grade $AB_2$ alloys have the advantage of relatively small pressure–concentration–temperature (PCT) hysteresis over conventional $AB_5$ alloys [11] through their flexible alloy compositional design [12]. This smaller PCT hysteresis contributes to higher round-trip energy efficiency. However, the self discharge in typical commercial-grade $AB_2$ alloys is higher compared to commercial-grade $AB_5$ alloys, which counteracts the PCT hysteresis advantage and can in turn lower the round-trip energy efficiency [13,14].

Vanadium, as a result of its high solubility in alkaline environment [11,15–17], causes an increase in shuttle redox reactions often associated with a lower charge retention [18]. Another disadvantage of the use of vanadium containing alloys is cost. The high cost of vanadium, even in the less-expensive form of ferrovanadium, encourages the elimination of vanadium from the alloy formula. However, the use of vanadium contributes positively to many of the alloy's electrochemical properties, such as higher storage capacity [19–24], easier activation [21], improved high-rate discharge ability (HRD) [25], and better cycle stability [26]. Therefore, a study in the compositions of vanadium-free $AB_2$ alloys is necessary to improve the self discharge of $AB_2$ alloys while maintaining all other performance characteristics. The optimization of contents of three key elements, Zr, Ti, and Ni, in the vanadium-free Laves phase $AB_2$ alloys is covered in this study.

## 2. Experimental setup

Induction melting from elementary raw materials was performed under an argon atmosphere in a 25 kg induction melting furnace using a MgO crucible, an alumina tundish, and a steel cylindrical mold. The ingots were first hydrided/dehydrided and mechanically crushed into −200 mesh powder. The chemical composition of each sample was examined by a Varian *Liberty* 100 inductively coupled plasma (ICP) system. A Philips *X'Pert Pro* X-ray diffractometer (XRD) was used to study the microstructure, and a JOEL-*JSM6320F* scanning electron microscope (SEM) with energy dispersive spectroscopy (EDS) capability was used to study the phase distribution and composition. PCT characteristics for each sample were measured using a Suzuki-Shokan multi-channel PCT system. In the PCT analysis, each sample was first activated by a two-hour thermal cycle between 300 °C and room temperature at 25 atm $H_2$ pressure. The PCT isotherms at 30 °C and 60 °C were then measured. Details of both electrode and cell preparation methods, as well as measurement methods, have been reported before [27–29].

## 3. Results and discussion

In our previous studies of vanadium-containing $AB_2$ MH alloys in NiMH battery applications, the $AB_{2.0}$ stoichiometric alloy ($B/A$ ratio equals 2.0) was selected [23,27,28,30–33,11,34,35] due to a combination of high capacity and good high-rate performance [36,37]. Vanadium is considered a hydride former as a result of

---

* Corresponding author. Tel.: +1 248 293 7000; fax: +1 248 299 4520.
*E-mail addresses:* kyoung@ovonic.com, kwoyoung@yahoo.com (K. Young).

0925-8388/$ – see front matter © 2011 Elsevier B.V. All rights reserved.
doi:10.1016/j.jallcom.2011.08.091

**Table 1**
Designed compositions (in bold) and ICP results in at.%. *e*/*a* is the average outer-shell electron density. *B*/*A* is the stoichiometry of the alloy.

| | | Ti | Zr | Cr | Mn | Co | Ni | Fe | *e*/*a* | *B*/*A* |
|---|---|---|---|---|---|---|---|---|---|---|
| Ti9 | **Design** | **9.0** | **28.0** | **8.0** | **15.0** | **5.0** | **35.0** | | **6.96** | **1.70** |
| | ICP | 8.9 | 28.4 | 7.8 | 14.8 | 5.0 | 35.0 | 0.06 | 6.95 | 1.68 |
| Ti10, Ni35 | **Design** | **10.0** | **27.0** | **8.0** | **15.0** | **5.0** | **35.0** | | **6.96** | **1.70** |
| | ICP | 9.6 | 26.7 | 7.8 | 15.3 | 5.3 | 35.1 | 0.07 | 6.98 | 1.75 |
| Ti11 | **Design** | **11.0** | **26.0** | **8.0** | **15.0** | **5.0** | **35.0** | | **6.96** | **1.70** |
| | ICP | 10.7 | 26.1 | 7.8 | 14.9 | 5.3 | 35.0 | 0.05 | 6.96 | 1.71 |
| Ti12 | **Design** | **12.0** | **25.0** | **8.0** | **15.0** | **5.0** | **35.0** | | **6.96** | **1.70** |
| | ICP | 11.7 | 25.2 | 7.9 | 15.1 | 5.2 | 34.9 | 0.06 | 6.97 | 1.71 |
| Ti13 | **Design** | **13.0** | **24.0** | **8.0** | **15.0** | **5.0** | **35.0** | | **6.96** | **1.70** |
| | ICP | 12.8 | 24.1 | 7.9 | 15.2 | 5.1 | 34.8 | 0.05 | 6.96 | 1.71 |
| Ni34 | **Design** | **10.0** | **28.0** | **8.0** | **15.0** | **5.0** | **34.0** | | **6.90** | **1.63** |
| | ICP | 10.0 | 28.1 | 7.9 | 15.0 | 4.9 | 34.0 | 0.08 | 6.90 | 1.62 |
| Ni36 | **Design** | **10.0** | **26.0** | **8.0** | **15.0** | **5.0** | **36.0** | | **7.02** | **1.78** |
| | ICP | 9.7 | 26.3 | 7.9 | 15.3 | 5.1 | 35.7 | 0.05 | 7.02 | 1.78 |
| Ni37 | **Design** | **10.0** | **25.0** | **8.0** | **15.0** | **5.0** | **37.0** | | **7.08** | **1.86** |
| | ICP | 10.0 | 25.1 | 7.7 | 15.4 | 5.0 | 36.6 | 0.07 | 7.06 | 1.85 |
| Ni38 | **Design** | **10.0** | **24.0** | **8.0** | **15.0** | **5.0** | **38.0** | | **7.14** | **1.94** |
| | ICP | 9.9 | 24.5 | 7.6 | 15.0 | 5.0 | 37.8 | 0.07 | 7.12 | 1.90 |

its ability to increase the metal–hydrogen bond strength in $AB_2$ MH alloys [23,38,39]. Removing vanadium from the composition would require other means of increasing the metal–hydrogen bond strength, and such can be achieved by either increasing the Zr/Ti ratio [27] or decreasing the *B*/*A* stoichiometric ratio [37]. Hence, two series of vanadium-free alloys were designed to address both approaches in this study: Ti-series, $Ti_xZr_{37-x}Cr_8Mn_{15}Co_5Ni_{35}$ ($x = 9$, 10, 11, 12, and 13) and Ni-series, $Ti_{10}Zr_{62-x}Cr_8Mn_{15}Co_5Ni_x$ ($x = 34$, 35, 36, 37, and 38). All compositions are designed to be hypo-stoichiometric to compensate for the reduction in capacity due to the elimination of vanadium with a fixed and varied *B*/*A* ratios in the Ti- and Ni-series, respectively.

In both series, changes in Ti and Ni are at the expense of Zr. Composition Ti10 in the first series is the same as Ni35 in the second series. The designed compositions are listed in Table 1. The average electron density (*e*/*a*) for each alloy, calculated from the average number of outer-shell electrons of the constituent elements, is listed in the same table. The *e*/*a* values in Ti-series are the same since both Ti and Zr have four outer-shell electrons and are near the lower border of C14/C15 threshold for stoichiometric $AB_{2.0}$ alloys [40,41]. However, as shown in the literature, other

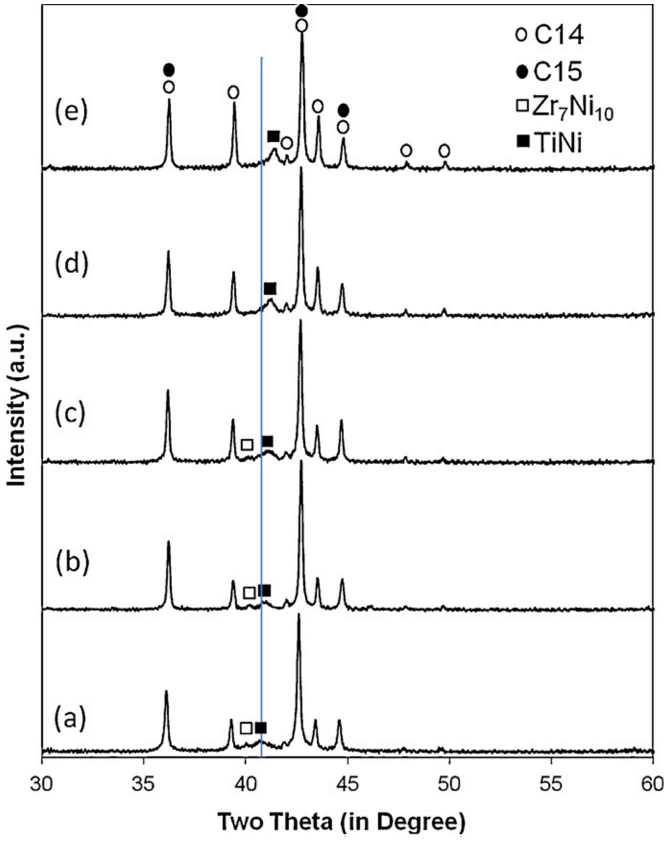

**Fig. 1.** XRD spectra using Cu-$K_\alpha$ as the radiation source for alloys Ti9 (a), Ti10 (b), Ti11 (c), Ti12 (d), and Ti13 (e). Vertical line is used to illustrate the shift of TiNi peak into higher angles.

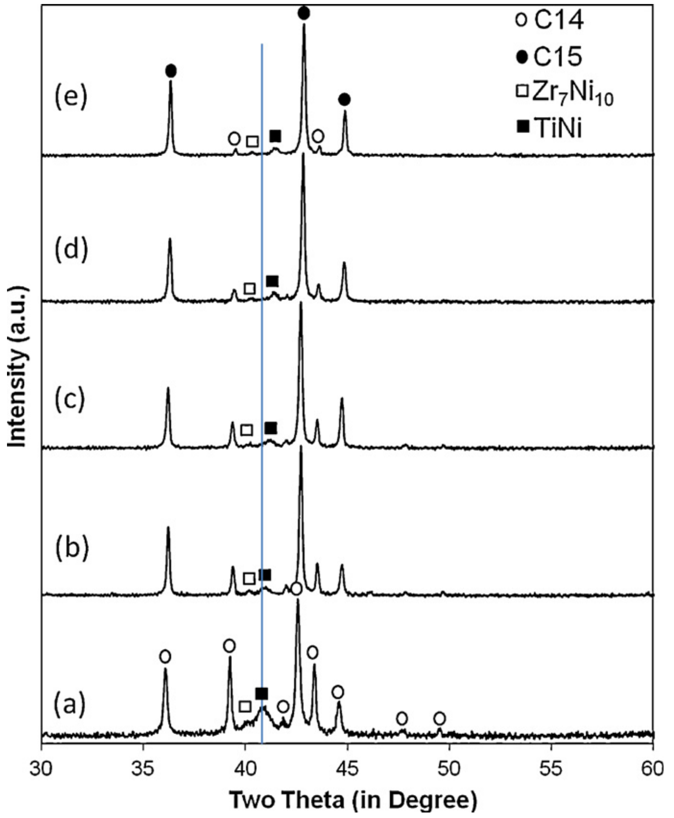

**Fig. 2.** XRD spectra using Cu-$K_\alpha$ as the radiation source for alloys Ni34 (a), Ni35 (b), Ni36 (c), Ni37 (d), and Ni38 (e). Vertical line is used to illustrate the shift of the TiNi peak into higher angles.

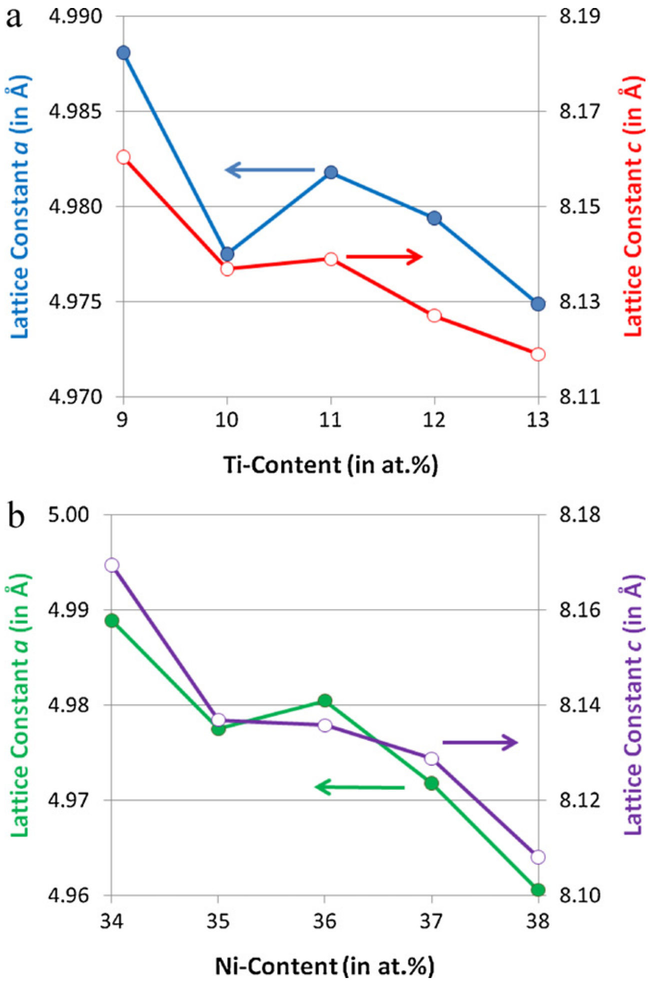

**Fig. 3.** The evolutions of lattice constants *a* and *c* for Ti- (a) and Ni-series (b) alloys as functions of compositional variation.

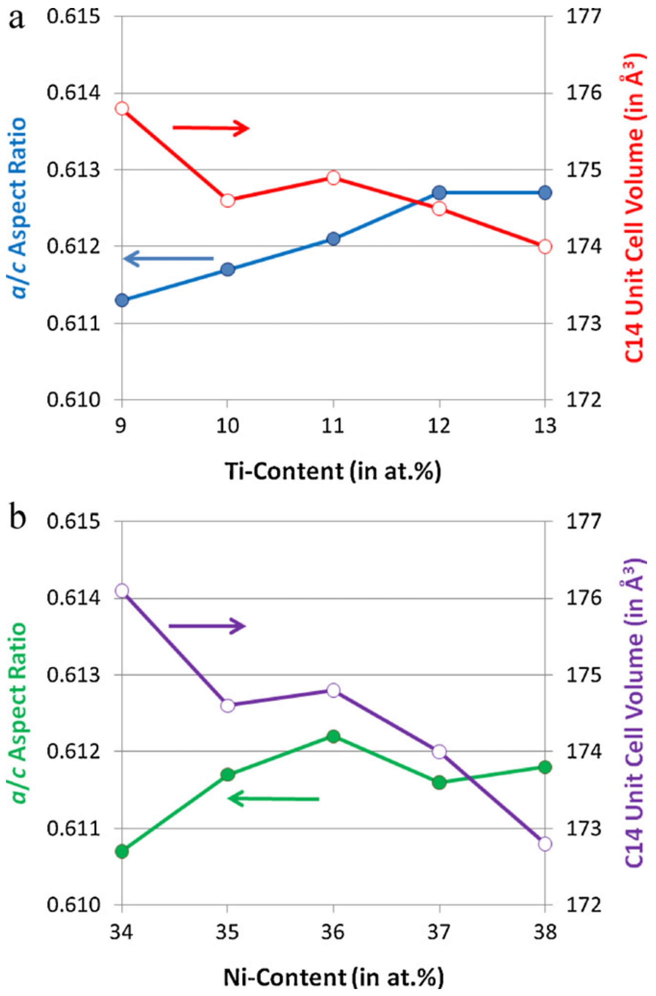

**Fig. 4.** Evolutions of *a*/*c* aspect ratio and C14 unit cell volume for Ti- (a) and Ni-series (b) alloys as functions of compositional variation.

than stoichiometry [40], the Ti/Zr ratio [42] also moves the C14/C15 threshold. Therefore, the final dominating phase cannot be predicted by *e*/*a* value alone. The *e*/*a* values in Ni-series increase and run across the C14/C15 threshold, and as a result, a shift from C14 dominating to C15 dominating structure is expected. The designed *B*/*A* stoichiometries are calculated and while the *B*/*A* ratio is fixed at 1.70 in the Ti-series, the *B*/*A* ratio increases from 1.63 to 1.94 in the Ni-series. The ICP results of all nine alloys are also listed in the same table. Minor deviation from the designed composition is observed in each sample, including a small Fe-pickup from the mold and a slight decrease in Ti due to the oxide slag formation.

### 3.1. XRD structure analysis

The XRD patterns of the five alloys in the Ti-series and the fives alloys in the Ni-series are shown in Figs. 1 and 2, respectively. Almost all peaks can be fitted to a hexagonal C14 ($MgZn_2$) structure with diffractions from a FCC C15 ($Cu_2Mg$) structure completely overlapping some of the C14 reflections. As the Ti-content increases in the Ti-series, the intensities of C14-only diffraction peaks increase. On the contrary, as the *B*/*A* ratio increases in the Ni-series, the intensities of C14-only diffraction peaks decrease, which validates the prediction from *e*/*a* values. The peak at around 41.5° corresponds to a B2 structured TiNi secondary phase. This phase is the precursor of a further solid-state transformation into

**Table 2**
Lattice constants *a* and *c*, *a*/*c* ratio, C14 lattice volume, full width at half of maximum of (1 0 3) reflection peak (in degree of 2$\theta$), corresponding crystallite size, and phase abundances calculated from XRD analysis.

| | *a* (Å) | *c* (Å) | *a*/*c* | $V_{C14}$ (Å$^3$) | FWHM (degree) | Crystallite size (Å) | C14 abund. (%) | C15 abund. (%) | $Zr_7Ni_{10}$ abund. (%) | TiNi abund. (%) |
|---|---|---|---|---|---|---|---|---|---|---|
| Ti9 | 4.9881 | 8.1604 | 0.6113 | 175.8 | 0.168 | 871 | 35 | 54 | 2.3 | 9 |
| Ti10, Ni35 | 4.9775 | 8.1369 | 0.6117 | 174.6 | 0.161 | 951 | 38 | 52 | 1.2 | 9 |
| Ti11 | 4.9818 | 8.1390 | 0.6121 | 174.9 | 0.148 | >1000 | 39 | 50 | 0.2 | 11 |
| Ti12 | 4.9794 | 8.1271 | 0.6127 | 174.5 | 0.161 | 949 | 49 | 40 | 0.3 | 11 |
| Ti13 | 4.9749 | 8.1190 | 0.6127 | 174.0 | 0.155 | >1000 | 56 | 33 | 0.0 | 12 |
| Ni34 | 4.9889 | 8.1695 | 0.6107 | 176.1 | 0.172 | 830 | 52 | 29 | 0.5 | 19 |
| Ni36 | 4.9805 | 8.1358 | 0.6122 | 174.8 | 0.169 | 859 | 34 | 60 | 0.8 | 6 |
| Ni37 | 4.9718 | 8.1288 | 0.6116 | 174.0 | 0.189 | 694 | 20 | 74 | 1.3 | 5 |
| Ni38 | 4.9606 | 8.1081 | 0.6118 | 172.8 | 0.147 | >1000 | 8.2 | 85 | 1.5 | 5 |

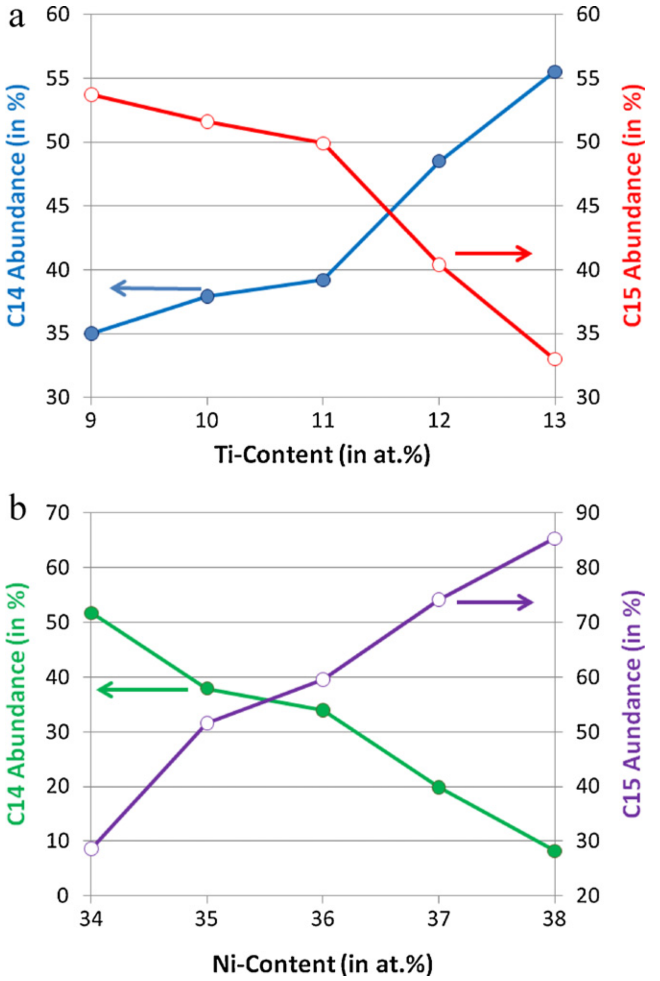

**Fig. 5.** Evolutions of C14 and C15 phase abundances for Ti- (a) and Ni-series (b) alloys as functions of compositional variation.

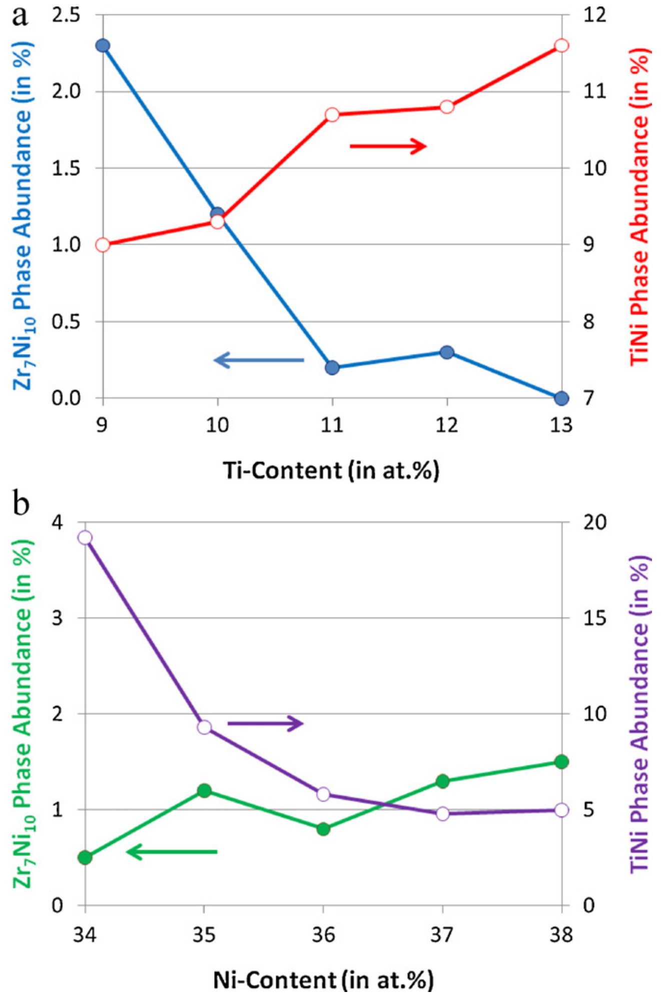

**Fig. 6.** Evolutions of $Zr_7Ni_{10}$ and TiNi phase abundances for Ti- (a) and Ni-series (b) alloys as functions of compositional variation.

$Zr_xNi_y$ type secondary phases [43,44]. The relatively wide peak of TiNi phase reveals its small crystallite size, and the observed peak position shifts from lower to higher angle as the Ti/Zr ratio increases in both series due to the increase in the amount of smaller sized Ti [33]. The alloys with lower Ti-content in the Ti-series and all alloys in the Ni-series contain a small trace of $Zr_7Ni_{10}$ phase according to their XRD spectra, which is very common in the multi-element $AB_2$ MH alloys [29,45–54].

All parameters obtained through the XRD analysis are listed in Table 2. The lattice constants *a* and *c* in the C14 structure for the Ti- and Ni-series alloys as functions of compositional variation are plotted in Fig. 3a and b, respectively. In the Ti-series, as the Ti-content increases, both *a* and *c* decrease due to the smaller radius of Ti with the exception of Ti10, which has an abnormally small lattice and does not follow the general trend. The same alloy, Ti10/Ni35 also falls off the general decreasing trend of both *a* and *c* as Ni-content increases in the Ni-series. The abnormal performance of Ti10/Ni35 may be attributed to its hyper-stoichiometric composition in the main $AB_2$ phase and will be elaborated on in the SEM/EDS session. The *a*/*c* aspect ratio, which is closely related to the pulverization rate during cycling [55–57], increases as the Ti-content increases in the Ti-series (Fig. 4a). In the Ni-series, *a*/*c* aspect ratio peaks at the mid composition (Ni36) (Fig. 4b). In general (except for Ti10/Ni35), the C14 unit cell volume decreases with higher Ti- and Ni-contents in the alloys. The crystallite size of each alloy was estimated by the Scherrer equation using the full-width at half of the maximum (FWHM) of the C14 (1 0 3) peak in the XRD pattern [58] and is listed in Table 2. The general trend of crystallite size as the Ti-content increases in the Ti-series is positive, while it is not obvious in the Ni-series.

The phase abundances were calculated using JADE 9 software and are listed in Table 2. The major phase abundances (C14 and C15) for the Ti- and Ni-series alloys are plotted in Fig. 5a and b, respectively. As the Ti-content increases in the Ti-series, the C14 phase abundance increases with a threshold reached at approximately 11.5% Ti. The trend of change in C14/C15 abundances is opposite in the Ni-series, where the C14 phase abundance decreases as the Ni-content increases with a threshold reached at approximately 35.5% ($e/a = 6.99$). The abundances of secondary phases for the Ti- and Ni-series alloys are plotted in Fig. 6a and b, respectively. The abundance of $Zr_7Ni_{10}$ phase decreases in the Ti-series and increases in the Ni-series as the Zr-content is reduced. The abundance of TiNi phase increases monotonically with the increase in Ti-content and decreases with the increase in Ni-content. Higher Ni-content increases the *B*/*A* stoichiometric ratio in the Ni-series and favors the formation of an $AB_2$ phase as compared to a TiNi phase with a *B*/*A* ratio of one.

### 3.2. SEM/EDS phase analysis

The microstructures for all alloys were studied by SEM and the back-scattering electron images (BEI) are presented in Fig. 7. The compositions in several areas, identified numerically in the

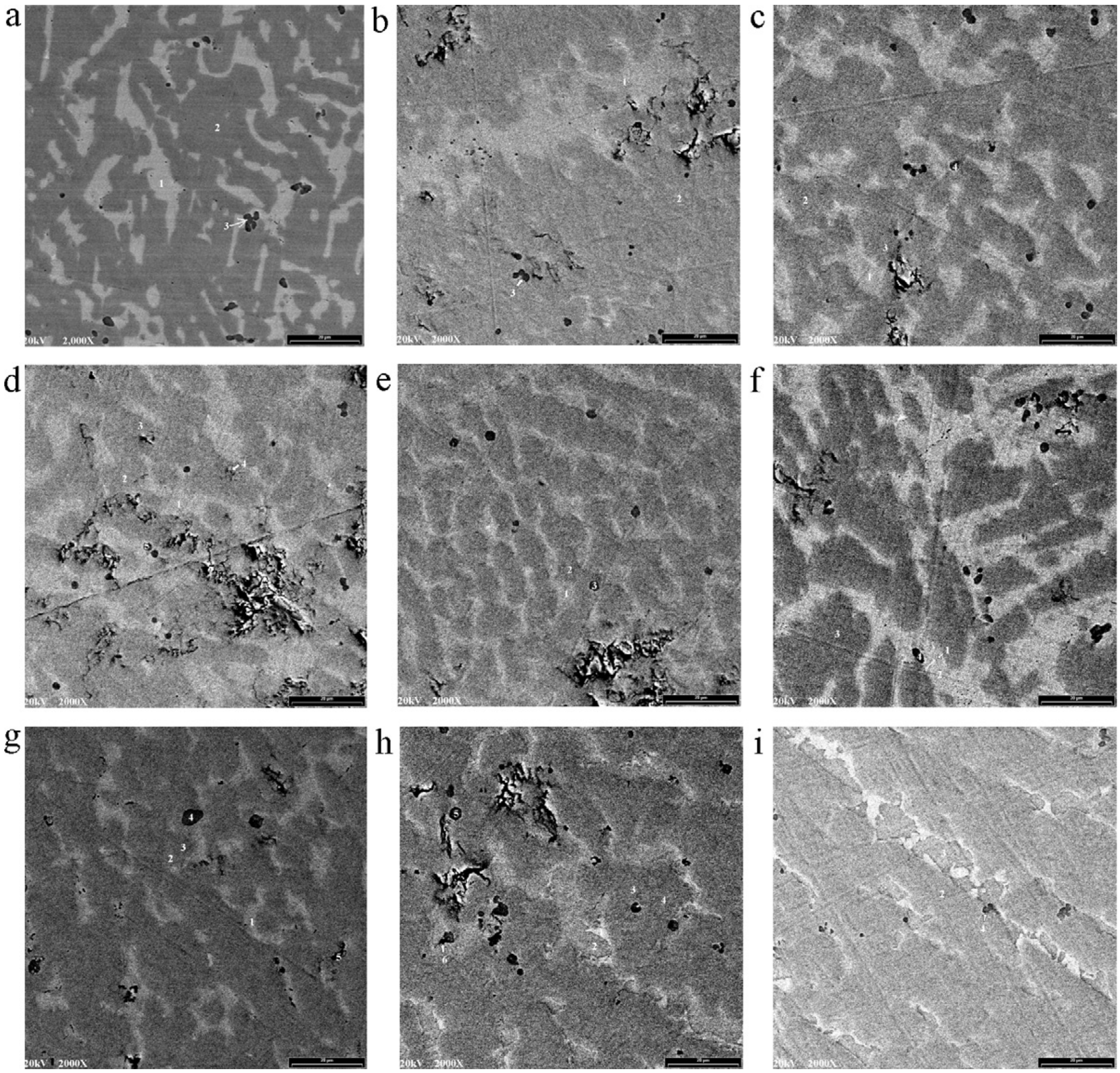

**Fig. 7.** SEM backscattering electron images for alloys Ti9 (a), Ti10 (b), Ti11 (c), Ti12 (d), Ti13 (e), Ni34 (f), Ni36 (g), Ni37 (h), and Ni38 (i).

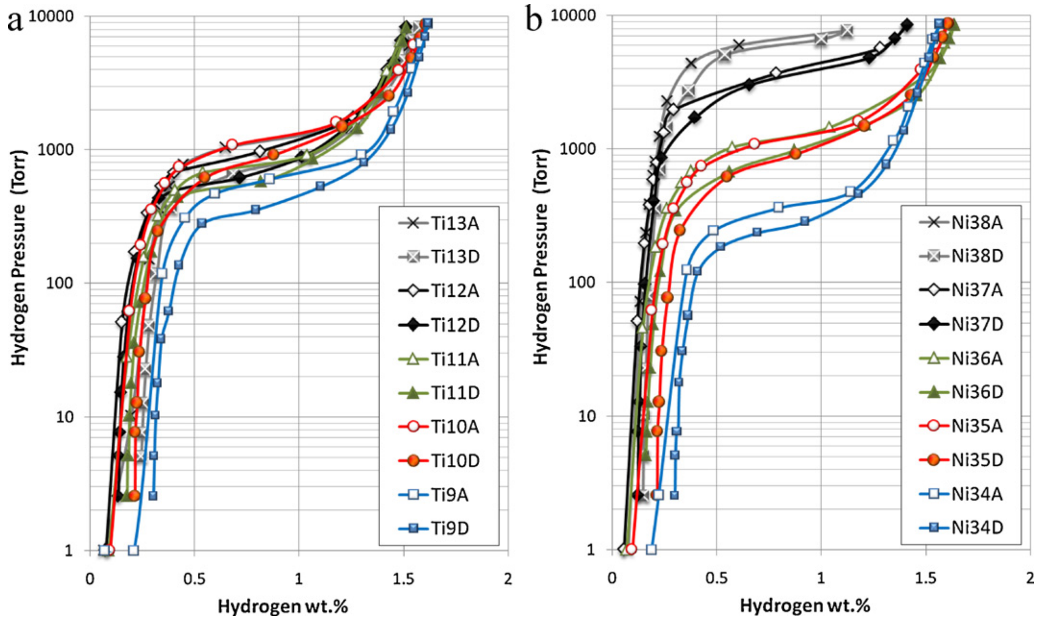

**Fig. 8.** PCT isotherms of Ti- (a) and Ni-series (b) alloys at 30 °C. Open and solid symbols are for absorption and desorption curves, respectively.

**Table 3**
Summary of EDS results. All compositions are in atomic percentages. The main phases are in bold.

| | | Ti | Zr | Cr | Mn | Co | Ni | *e*/*a* | *B*/*A* | Phase |
|---|---|---|---|---|---|---|---|---|---|---|
| Ti9 | Fig. 7a-1 | 13.2 | 30.9 | 0.6 | 3.4 | 4.2 | 47.8 | 7.20 | 1.27 | $TiNi/Zr_7Ni_{10}$ |
| | Fig. 7a-2 | **8.6** | **25.1** | **7.3** | **18.3** | **6.1** | **34.7** | **7.09** | **1.97** | **$AB_2$** |
| | Fig. 7a-3 | 3.2 | 86.3 | 0.0 | 1.0 | 0.0 | 9.4 | 4.59 | 0.12 | $ZrO_2$ |
| Ti10, Ni35 | Fig. 7b-1 | 15.8 | 31.4 | 0.2 | 3.4 | 3.1 | 46.0 | 7.02 | 1.12 | TiNi |
| | Fig. 7b-2 | **9.1** | **22.4** | **7.2** | **19.2** | **4.3** | **37.8** | **7.20** | **2.17** | **$AB_2$** |
| | Fig. 7b-3 | 1.2 | 92.6 | 0.5 | 1.6 | 0.4 | 3.7 | 4.30 | 0.07 | $ZrO_2$ |
| Ti11 | Fig. 7c-1 | 17.2 | 29.8 | 0.4 | 3.6 | 3.7 | 45.3 | 7.02 | 1.13 | TiNi |
| | Fig. 7c-2 | 9.3 | 26.7 | 10.0 | 18.5 | 5.1 | 30.5 | 6.84 | 1.78 | $AB_2$ |
| | Fig. 7c-3 | **8.3** | **26.9** | **14.5** | **19.3** | **5.2** | **25.8** | **6.68** | **1.84** | **$AB_2$** |
| | Fig. 7c-4 | 3.6 | 84.1 | 1.0 | 2.3 | 0.6 | 8.3 | 4.61 | 0.14 | $ZrO_2$ |
| Ti12 | Fig. 7d-1 | 19.3 | 26.7 | 0.4 | 3.8 | 3.8 | 46.0 | 7.07 | 1.17 | TiNi |
| | Fig. 7d-2 | **9.6** | **24.1** | **13.6** | **19.8** | **5.1** | **27.8** | **6.79** | **1.97** | **$AB_2$** |
| | Fig. 7d-3 | 11.3 | 24.6 | 5.4 | 16.1 | 5.1 | 37.5 | 7.10 | 1.79 | $AB_2$ |
| | Fig. 7d-4 | 10.6 | 24.6 | 9.6 | 18.7 | 5.1 | 31.5 | 6.90 | 1.84 | $AB_2$ |
| | Fig. 7d-5 | 6.5 | 68.6 | 1.8 | 5.1 | 1.7 | 16.2 | 5.24 | 0.33 | $ZrO_2$ |
| Ti13 | Fig. 7e-1 | 18.3 | 26.7 | 0.4 | 4.0 | 3.6 | 47.0 | 7.13 | 1.22 | TiNi |
| | Fig. 7e-2 | **11.1** | **24.0** | **12.5** | **19.4** | **4.8** | **28.2** | **6.76** | **1.85** | **$AB_2$** |
| | Fig. 7e-3 | 4.3 | 71.7 | 1.2 | 4.7 | 1.9 | 16.3 | 5.24 | 0.32 | $ZrO_2$ |
| Ni34 | Fig. 7f-1 | 13.3 | 32.7 | 0.2 | 3.7 | 2.9 | 47.3 | 7.10 | 1.18 | TiNi |
| | Fig. 7f-2 | 14.4 | 31.1 | 0.2 | 3.8 | 3.6 | 46.9 | 7.11 | 1.20 | TiNi |
| | Fig. 7f-3 | **6.9** | **25.9** | **18.6** | **21.6** | **5.1** | **21.9** | **6.59** | **2.05** | **$AB_2$** |
| | Fig. 7f-4 | 7.0 | 69.1 | 0.2 | 2.0 | 1.3 | 20.3 | 5.34 | 0.31 | $ZrO_2$ |
| Ni36 | Fig. 7g-1 | 15.9 | 28.0 | 1.4 | 4.9 | 3.5 | 46.3 | 7.13 | 1.28 | TiNi |
| | Fig. 7g-2 | 8.1 | 25.5 | 10.0 | 19.4 | 5.4 | 31.5 | 6.94 | 1.97 | $AB_2$ |
| | Fig. 7g-3 | **10.5** | **25.8** | **6.6** | **14.1** | **4.3** | **38.7** | **7.09** | **1.75** | **$AB_2$** |
| | Fig. 7g-4 | 0.5 | 96.5 | 0.3 | 0.5 | 0.1 | 2.0 | 4.14 | 0.03 | $ZrO_2$ |
| | Fig. 7g-5 | 0.4 | 96.5 | 0.3 | 0.5 | 0.1 | 2.2 | 4.16 | 0.03 | $ZrO_2$ |
| Ni37 | Fig. 7h-1 | 17.8 | 25.2 | 1.1 | 5.7 | 3.3 | 47.0 | 7.18 | 1.33 | $TiNi/Zr_7Ni_{10}$ |
| | Fig. 7h-2 | 18.4 | 25.1 | 0.3 | 3.8 | 3.1 | 49.3 | 7.23 | 1.30 | $TiNi/Zr_7Ni_{10}$ |
| | Fig. 7h-3 | **9.1** | **24.2** | **7.8** | **16.3** | **4.7** | **37.8** | **7.14** | **2.00** | **$AB_2$** |
| | Fig. 7h-4 | 7.8 | 24.5 | 10.4 | 18.7 | 5.2 | 33.4 | 7.03 | 2.10 | $AB_2$ |
| | Fig. 7h-5 | 0.9 | 92.6 | 0.6 | 1.8 | 0.4 | 3.6 | 4.30 | 0.07 | $ZrO_2$ |
| | Fig. 7h-6 | 19.1 | 58.0 | 0.4 | 2.2 | 1.1 | 19.2 | 5.28 | 0.30 | $ZrO_2$ |
| Ni38 | Fig. 7i-1 | 11.7 | 29.3 | 0.1 | 2.0 | 1.1 | 55.7 | 7.46 | 1.44 | $Zr_7Ni_{10}$ |
| | Fig. 7i-2 | **7.9** | **24.0** | **9.6** | **15.9** | **5.4** | **37.2** | **7.17** | **2.13** | **$AB_2$** |
| | Fig. 7i-3 | 20.4 | 23.5 | 0.2 | 4.2 | 3.1 | 48.6 | 7.20 | 1.28 | $TiNi/Zr_7Ni_{10}$ |
| | Fig. 7i-4 | 8.0 | 63.2 | 0.9 | 4.7 | 1.3 | 22.0 | 5.55 | 0.41 | $ZrO_2$ |

micrographs, were studied by EDS and are listed in Table 3. The *e*/*a* and *B*/*A* (stoichiometric number) values were also calculated and are listed in the same table. In the Ti-series, the brightest regions are $TiNi/Zr_7Ni_{10}$ phases with *B*/*A* ratio between 1.0 and 1.42, the darkest regions are $ZrO_2$ phase, and the regions with in between shades are $AB_2$ phases. Cr and Mn mainly reside in the $AB_2$ phases. In general, as the Ti-content increases, the abundance of $TiNi/Zr_7Ni_{10}$ phase increases and its average size decreases and those of $ZrO_2$ phase remain unchanged. Although the *e*/*a* values of the overall average composition in the Ti-series alloys are the same (6.96), the actual *e*/*a* values in the $AB_2$ phases, as identified by EDS analysis, decrease monotonically from 7.09 to 6.76 with increasing Ti-content. This explains the increase in C14 phase abundance found by XRD analysis (Table 2) as the Ti-content increases in the Ti-series. The *B*/*A* stoichiometric numbers in the main $AB_2$ phases in the Ti-series alloys are similar (1.84–1.97) with the exception of Ti10 (2.17). The extremely hyper-stoichiometry in Ti10 $AB_2$ phases decreases the lattice constants, and this finding confirms the XRD result. In the Ni-series, the abundance and size of $TiNi/Zr_7Ni_{10}$ and $ZrO_2$ phases decrease as the Ni-content increases. Both the *e*/*a* values from the average composition and from the main $AB_2$ phases increase as the Ni-content increases, and therefore the C15 phase becomes more dominant as shown in the XRD analysis. The *B*/*A* stoichiometric numbers in the Ni-series do not show any clear trend (2.05, 2.17, 1.75, 2.00, and 2.13). Within the alloys in this series, Ni35 shows the highest *B*/*A* stoichiometry, which explains the relatively small lattice constants found by XRD analysis.

### 3.3. *Gaseous phase study*

Gaseous phase hydrogen storage properties of the alloys were studied by PCT. The resulting absorption and desorption isotherms, measured at 30 °C, for the Ti- and Ni-series alloys are shown in Fig. 8a and b, respectively. The information obtained from the PCT study is summarized in Table 4. In the Ti-series, the plateau pressure increases as the Ti-content increases with the exception of Ti10. This result is in agreement with the general trend of reduction in lattice constants *a* and *c* as the Ti-content increases. The relatively high plateau pressure of Ti10 is related to the high level of hyper-stoichiometry in the main $AB_2$ phases. In the Ni-series, the desorption plateau pressure increases with the increased Ni-content at the expense of Zr. The slope factor (SF), defined as the ratio of the storage capacity between 76 and 3800 Torr to the total capacity, can be used to determine the degree of disorder in the alloy [28,33]. The SF value first increases and then decreases slightly as the Ti-content increases in the Ti-series. Same value increases monotonically as the Ni-content increases in the Ni-series. In the Ni38 alloy, the plateau pressure is so high and cannot be covered entirely by the PCT test range, therefore the SF of Ni38 cannot be calculated.

The hysteresis of the PCT isotherm, listed in Table 4, is defined as $\ln(P_a/P_d)$, where $P_a$ and $P_d$ are the absorption and desorption equilibrium pressures, respectively. As the Ti-content increases in the Ti-series, the PCT hysteresis increases monotonically with the exception of Ti10 that shows an abnormally large hysteresis. In the Ni-series, the hysteresis of the three alloys with lower Ni-content are similar and larger than those of the two alloys with higher

**Table 4**
Summary of gas phase properties (plateau pressure, slope factor, hysteresis, total capacity, reversible capacity, and changes in enthalpy and entropy), results from half-cell measurement (pre-charge, 50 mA/g high-rate discharge capacity, 5 mA/g full discharge capacity, and high-rate discharge ability), and results from full-cell measurement (cycle life, charge retention, specific power, and low-temperature performance).

| | Des. pressure @0.75%, 30 °C (Torr) | Slope factor @30 °C (%) | PCT hysteresis@0.50%, 30 °C | Total cap. @30 °C (wt.%) | Rev. cap. @30 °C (wt.%) | $-\Delta H$ (kJ/mol) | $-\Delta S$ (J/mol K) | Pre-charge (mAh/g) | Cap. @50 mA/g (mAh/g) | Full cap. @5 mA/g (mAh/g) | HRD | 70% cycle life | 30 days charge retention (%) | Room temp. specific power (W/kg) | 0 °C specific power (W/kg) | Cap. @ − 10 °C, 0.5 C (mAh/g) |
|---|---|---|---|---|---|---|---|---|---|---|---|---|---|---|---|---|
| Ti9 | 340 | 0.73 | 0.18 | 1.62 | 1.32 | 35.5 | 110 | 1 | 332 | 360 | 0.92 | 230 | 72 | 173 | 114 | 82 |
| Ti10, Ni35 | 795 | 0.84 | 0.42 | 1.61 | 1.40 | 31.5 | 104 | 29 | 341 | 374 | 0.91 | 305 | 69 | 171 | 124 | 90 |
| Ti11 | 530 | 0.82 | 0.29 | 1.51 | 1.33 | 32.1 | 103 | 2 | 346 | 370 | 0.94 | 145 | 35 | 167 | 113 | 88 |
| Ti12 | 640 | 0.87 | 0.37 | 1.51 | 1.37 | 33.9 | 110 | 9 | 347 | 371 | 0.94 | 130 | 29 | 140 | 107 | 87 |
| Ti13 | 700 | 0.79 | 0.57 | 1.58 | 1.34 | 32.7 | 107 | 12 | 344 | 370 | 0.93 | 100 | 28 | 174 | 130 | 83 |
| Ni34 | 240 | 0.77 | 0.40 | 1.56 | 1.26 | 36.7 | 102 | 3 | 321 | 356 | 0.90 | 140 | 23 | 120 | 84 | 90 |
| Ni36 | 830 | 0.87 | 0.42 | 1.63 | 1.47 | 30.8 | 102 | 8 | 344 | 367 | 0.94 | 280 | 44 | 157 | 110 | 89 |
| Ni37 | 3200 | 0.90 | 0.19 | 1.41 | 1.29 | 27.3 | 102 | 8 | 293 | 310 | 0.95 | 260 | 42 | 134 | 103 | 78 |
| Ni38 | 5800 | – | 0.20 | 1.12 | 0.98 | 24.8 | 108 | 18 | 176 | 187 | 0.94 | 110 | 43 | 25 | 25 | 82 |

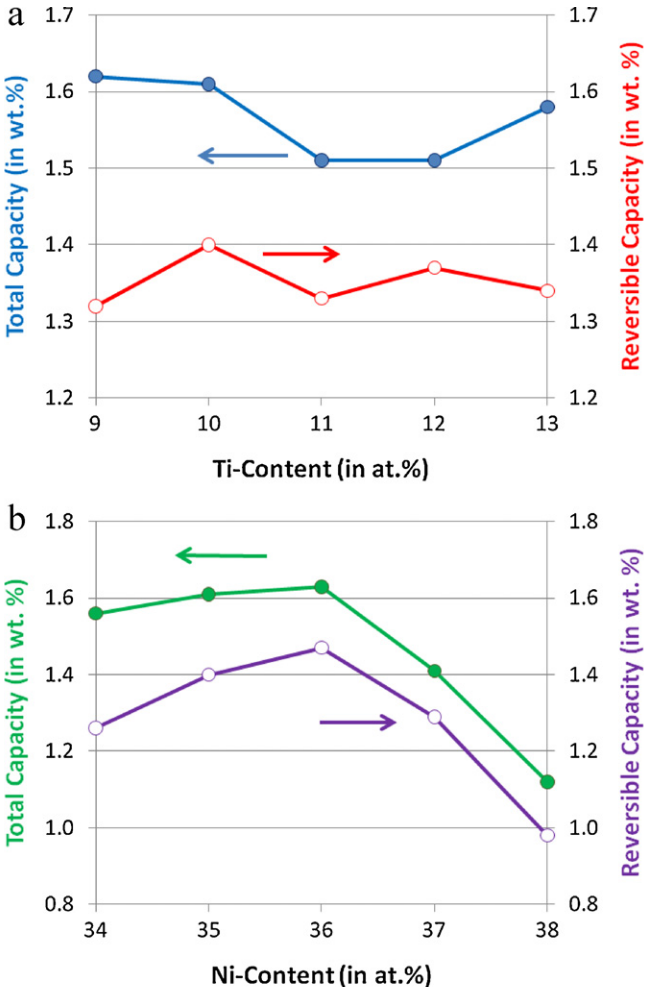

**Fig. 9.** Gas phase total and reversible hydrogen storage capacities of Ti- (a) and Ni-series (b) alloys as functions of compositional variation.

Ni-content. Both the maximum and reversible hydrogen storage capacities for the Ti- and Ni-series alloys are plotted in Fig. 9a and b, respectively, as functions of compositional variation. In the Ti-series, all alloys show similar results in both quantities despite the large difference in the unit cell volumes. Alloy Ti10 has the highest reversible hydrogen storage capacity in the Ti-series due to the hyper-stoichiometry in its main $AB_2$ phase. In the Ni-series, both capacities first increase and then decrease with increasing Ni-content. The highest maximum and reversible hydrogen storage capacities in the Ni-series are observed in the mid composition, Ni36. Desorption equilibrium pressures at 0.75% storage capacity, measured at 30 and 60 °C, were used to calculate changes in enthalpy ($\Delta H$) and entropy ($\Delta S$) using the equation

$$\Delta G = \Delta H - T\Delta S = RT \ln P \qquad (1)$$

where $R$ is the ideal gas constant and $T$ is the absolute temperature. The results of these calculations are listed in Table 4. $\Delta H$ values have similar trends to desorption plateau pressure for both alloy series. $\Delta S$ values are about the same for all alloys in both series, which is close to the $\Delta S$ between hydrogen in gas and in solid [59].

### 3.4. Electrochemical measurement

The discharge capacity of each alloy was measured in a flooded-cell configuration against a partially pre-charged sintered positive electrode. Before the half-cell measurement, each MH electrode was pre-activated in a 30% KOH solution at 100 °C for 4 h.

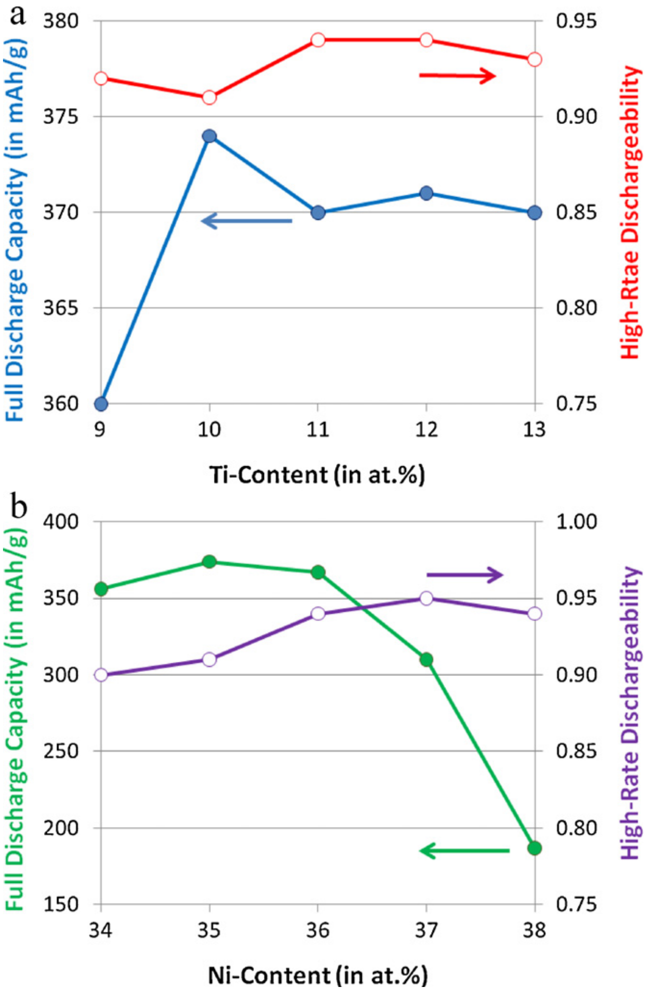

**Fig. 10.** Electrochemical full discharge capacity and high-rate discharge ability of Ti- (a) and Ni-series (b) alloys as functions of compositional variation.

Pre-activated electrodes typically exhibit a small amount of initial discharge capacity before the first charge input. This initial discharge capacity is considered to be due to the hydrogen generation and absorption resulted from metal oxidation when exposed to electrolyte at elevated temperatures and can be used to quantify the ease of activation of the individual alloy [60]. A higher initial discharge capacity can be correlated to an easier oxidation/activation of the alloy. The amount of pre-charge in mAh/g for each alloy is listed in Table 4. In the Ti-series, the amount of pre-charge capacity increases with rising Ti-content with the exception of alloy Ti10. Higher Ti-content replacing Zr allows easier surface activation of the alloy [61]. The hyper-stoichiometry in the main $AB_2$ phases may be related to the corrosion resistance to KOH and requires further investigation. In the Ni-series, the activation becomes easier with higher Ni-content.

The first cycle discharge capacity after activation was measured at a relatively high rate, 50 mA/g, and the remaining capacity was extracted at a lower rate, 5 mA/g. The ratio of the capacities obtained from these two rates is defined as the half-cell HRD. All three quantities are listed in Table 4. The full discharge capacity and HRD value are plotted against the chemical compositions in Fig. 10a and b, respectively. In the Ti-series alloys, both the full discharge capacity and HRD increase with increasing Ti-content with the exception of Ti10. Alloy Ti10 exhibits both the highest full discharge capacity and the lowest HRD among all Ti-series alloys, which is contradictory to the largest gas phase reversible storage capacity in Ti10. In the Ni-series alloys, both the full discharge capacity and HRD first increase and then decrease with higher Ni-content. The largest full discharge capacity and HRD occur at Ni35 and Ni37, respectively. While in most of earlier studies, the electrochemical and gaseous phase storage capacities are closely related, in this case of highly disordered vanadium-free $AB_2$ alloys there is not much correlation, and even contradicting results were sometimes observed.

Four important NiMH technical parameters (cycle life, charge retention, specific power, and low-temperature performance) for the MH electrode made from each alloy are listed in Table 4. The number of cycles required to reach 70% of the original capacity in both series, first increase and then decrease with reducing Zr-content. The highest cycle life was obtained from the Ti10/Ni35 alloy among all alloys in both series, which contradicts the predictions from the *a*/*c* aspect ratio and PCT hysteresis. Therefore, the failure mechanism of these vanadium-free $AB_2$ alloys is not the result of pulverization in the main phase. Further analysis of the battery after the end of cycle life indicates that the difference in plateau pressures of the constituent phases causes pulverization among phases by wedge effect. As seen from a cross-section SEM-BEI (Fig. 11a) of a negative electrode made of Ti10 alloy in a sealed Ni/MH battery after 305 cycles (end of life), only large size grains

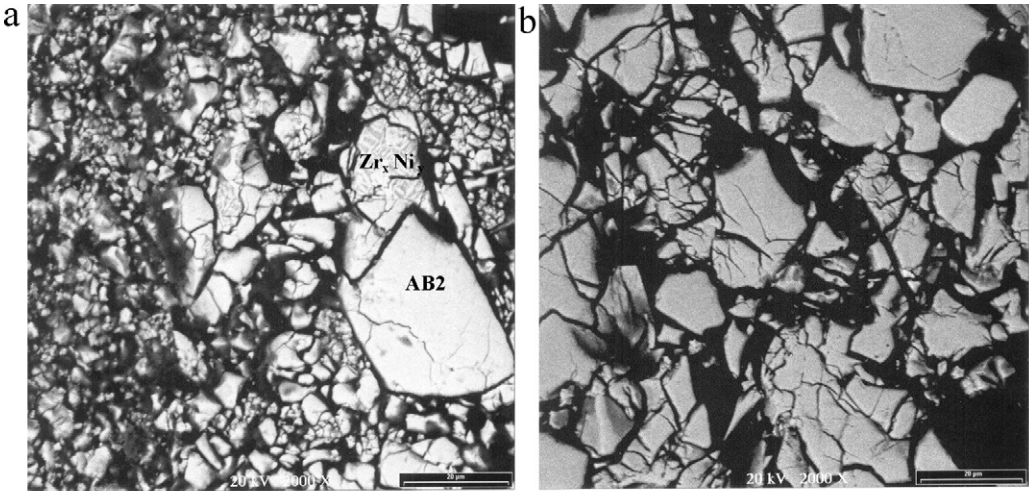

**Fig. 11.** Cross-section SEM backscattering electron images of negative electrodes made from vanadium-free Ti10 (a) and vanadium-containing V177 (b) MH alloys taken from Ni/MH batteries at the end of cycle life.

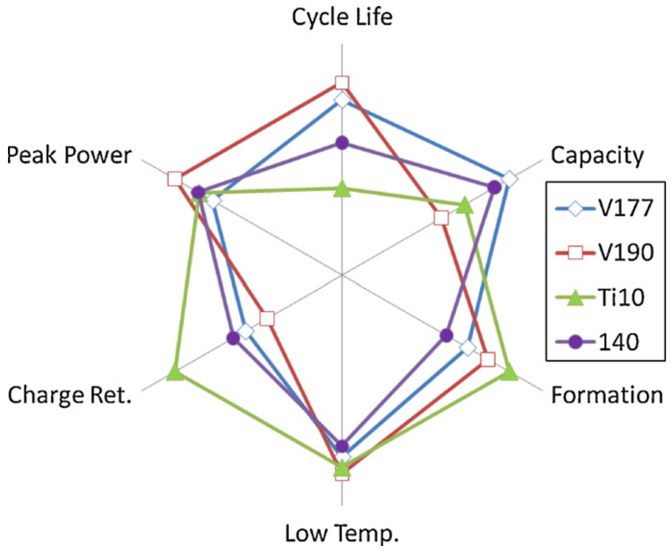

**Fig. 12.** Radar graph comparing the performances of vanadium-containing V177 and V190, and vanadium-free Ti10 and 140 MH electrode materials in Ni/MH battery.

from both the main $AB_2$ and secondary $Zr_xNi_y$ phases remain intact. Other smaller grain phases broke into even smaller pieces. This is different from that of a typical vanadium-containing alloy at the end of its cycle life (around 600 cycles) (Fig. 11b), in which the composition is more uniform across the whole area and pulverization is not as severe. The typical failure mode of vanadium-containing alloys is the dry-out of electrolyte due to cell venting during cycling.

The 30-day charge retention in the Ti-series decreases with higher Ti-content, while charge retention first increases and then decreases in the Ni-series. The best charge retention was obtained from alloy Ti9 among all alloys in both series. The specific power measured at room temperature first decreases and then increases with increasing Ti-content in the Ti-series and decreases with increasing Ni-content in the Ni-series. This result is not consistent with the half-cell HRD outcome. While in sealed cell, the amount of electrolyte is limited, so the surface of the MH alloy is semi-starved. Furthermore, the sealed cell pressure is much higher than one atmosphere. These conditions are very different from the completely flooded configuration in the half-cell measurement. Similar disagreement between high-rate performance measured in half-cell and full-cell was reported in our studies of various modifiers on $AB_2$ MH alloys [34,35,62]. Combining the results from all three measurements, alloy Ti10 (Ni35) has the best high-rate and low-temperature capability.

## 4. Summary

An optimization of the Ti, Zr, and Ni-contents in vanadium-free hypo-stoichiometric $AB_2$ metal hydride alloys was performed. While alloys with low Ti-content (<10 at.%) have too strong metal–hydrogen bond strength and consequently lower reversible storage capacity, the bond strengths in alloys with higher Ti-content (>10 at.%) are too weak and cause degradations in total gaseous phase and electrochemical discharge capacities. Varying Ni-content in the alloys has similar effect to changing the metal–hydrogen bond strength. As a result, alloy Ti10/Ni35, with a composition of $Ti_{10}Zr_{27}Cr_8Mn_{15}Co_5Ni_{35}$, is identified to be the most optimized in this study based on the high capacity, good high-rate capability, low self-discharge, superior low-temperature performance, and excellent cycle stability owing to its good balance in metal–hydrogen bond strength and the highly hyper-stoichiometric nature in its $AB_2$ phases. Furthermore, in order to illustrate the fundamental difference in NiMH battery performance between vanadium-containing and vanadium-free $AB_2$ Laves phase MH alloys, four alloys were compared in the radar graph (Fig. 12). Both the high-capacity V177 ($Ti_{12}Zr_{21.5}V_{10}Ni_{40.2}Co_{1.5}Cr_{8.5}Mn_{5.6}Al_{0.4}Sn_{0.3}$) and the high-power V190 ($Ti_{12}Zr_{21.5}V_{10}Ni_{40.2}Co_{5.0}Cr_{5.5}Mn_{5.1}Al_{0.4}Sn_{0.3}$) vanadium-containing stoichiometric alloys were from a comparison study of C14 and C15 phases [11]. Alloy 140 ($Ti_5Zr_{30}Cr_9Mn_{19}Co_5Ni_{32}$) is a high-capacity vanadium-free alloy used as the base alloy for a hydrogen annealing study [62] and a modifier study [63]. From the comparison, the main performance differences between alloys with and without vanadium are identified in the areas of charge retention and cycle life. Vanadium-free alloys have better charge retention performance but inferior cycle life.

## References

[1] M. Fetcenko, K. Young, Proceedings of Conference of International Battery Frontier, Beijing, China, June 23–25, China Industrial Association of Power Source, 2010, p. 259.
[2] K. Young, M. Fetcenko, C. Fierro, Proceedings of 2011 IEEE Power & Energy Society General Meeting, Detroit, USA, July 24–29, IEEE, NY, USA, 2011.
[3] M. Fetcenko, Proceedings of Pacific Power Source Symposium 2011, Hawaii, USA, January 10–14, 2011.
[4] M. Fetcenko, Proceedings of 28th International Battery Seminar & Exhibit, Fort Lauderdale, FL, USA, March 14–17, 2011.
[5] Y. Liu, H. Pan, M. Gao, H. Miao, Y. Lei, Q. Wang, Int. J. Hydrogen Energy 33 (2008) 124.
[6] Y. Liu, H. Pan, M. Gao, Y. Zhu, Y. Lei, Q. Wang, Electrochim. Acta 49 (2004) 545.
[7] H. Pan, Y. Liu, M. Gao, Y. Zhu, Y. Lei, Q. Wang, J. Electrochem. Soc. 151 (2004) A374.
[8] Y. Liu, H. Pan, M. Gao, R. Li, Y. Lei, J. Alloys Compd. 376 (2004) 296.
[9] H. Pan, R. Li, M. Gao, Y. Liu, Y. Lei, Q. Wang, Int. J. Hydrogen Energy 31 (2006) 1185.
[10] S. Yasuoka, Y. Magari, T. Murata, T. Tanaka, J. Ishida, H. Nakamura, T. Nohma, M. Kahara, Y. Baba, H. Teraoka, J. Power Sources 156 (2006) 662.
[11] K. Young, M.A. Fetcenko, B. Huang, R.K. Regmi, G. Lawes, Y. Liu, J. Alloys Compd. 506 (2010) 831.
[12] G. Sandrock, J. Alloys Compd. 293–295 (1999) 877.
[13] X.G. Yang, B.Y. Liaw, in: R.J. Jungst, J.W. Weidner, B. Liaw, K. Nechev (Eds.), Proceedings of the Power Source Modeling symposium, Fall 2002 ECS Meeting, Salt Lake City, Utah, Electrochemical Society, 2002, p. 87.
[14] A.K. Shukla, S.K. Martha, Resonance (July) (2001) 52.
[15] H.J. Chuang, S.L.I. Chan, J. Power Sources 77 (1999) 159.
[16] M. Wu, H. Wu, Y. Wang, C. Wan, J. Alloys Compd. 302 (2000) 248.
[17] B. Knosp, L. Vallet, Ph. Blanchard, J. Alloys Compd. 293–295 (1999) 770.
[18] X. Yang, B.Y. Liaw, J. Electrochem. Soc. 151 (2004) A137.
[19] S.V. Mitrokhin, T.N. Bezuglaya, V.N. Verbetsky, J. Alloys Compd. 330–332 (2002) 146.
[20] S. Li, S. Ji, J. Sun, J. Dalian Maritime Univ. 29 (2003) 79.
[21] X. Yu, B. Xia, Z. Wu, N. Zu, Mater. Sci. Eng. A373 (2004) 303.
[22] J.C. Wang, R.H. Yu, Q. Liu, Mater. Sci. Technol. 13 (2005) 166.
[23] K. Young, M.A. Fetcenko, F. Li, T. Ouchi, J. Koch, J. Alloys Compd. 468 (2009) 482.
[24] S.S. Makridis, A. Ioannidou, E. Zupanic, A. Prodan, E.S. Kikkinides, A.K. Stubos, Mater. Sci. Forum 636–637 (2010) 887.
[25] H.A. Peretti, A. Visintin, L.V. Mogni, H.L. Corso, J.A. Gamboa, D. Serafini, W.E. Triaca, J. Alloys Compd. 354 (2003) 181.
[26] B.H. Liu, Z.P. Li, S. Suda, J. Electrochem. Soc. 149 (2002) A537.
[27] K. Young, M.A. Fetcenko, T. Ouchi, F. Li, J. Koch, J. Alloys Compd. 464 (2008) 238.
[28] K. Young, T. Ouchi, J. Koch, M.A. Fetcenko, J. Alloys Compd. 477 (2009) 749.
[29] K. Young, M.A. Fetcenko, J. Koch, K. Morii, T. Shimizu, J. Alloys Compd. 486 (2009) 559.
[30] K. Young, M.A. Fetcenko, T. Ouchi, F. Li, J. Koch, J. Alloys Compd. 469 (2009) 406.
[31] K. Young, T. Ouchi, M.A. Fetcenko, J. Alloys Compd. 476 (2009) 774.
[32] K. Young, T. Ouchi, B. Reichman, W. Mays, R. Regmi, G. Lawes, M.A. Fetcenko, A. Wu, J. Alloys Compd. 489 (2010) 202.
[33] K. Young, R. Regmi, G. Lawes, T. Ouchi, B. Reichman, M.A. Fetcenko, A. Wu, J. Alloys Compd. 490 (2010) 282.
[34] K. Young, T. Ouchi, B. Huang, B. Reichman, M.A. Fetcenko, J. Power Sources 196 (2011) 8815.
[35] K. Young, T. Ouchi, B. Huang, B. Reichman, M.A. Fetcenko, Int. J. Hydrogen Energy (2011), doi:10.1016/j.ijhydene.2011.06.117.
[36] K. Young, B. Huang, J. Yang, M.A. Fetcenko, Int. J. Hydrogen Energy 36 (2011) 11137.
[37] K. Young, T. Ouchi, J. Nei, M.A. Fetcenko, Int. J. Hydrogen Energy 36 (2011) 11146.
[38] S.R. Ovshinsky, M.A. Fetcenko, J. Ross, Science 260 (1993) 176.
[39] K. Young, T. Ouchi, M.A. Fetcenko, W. Mays, B. Reichman, Int. J. Hydrogen Energy 34 (2009) 8695.
[40] Z. Shi, S. Chumbley, F.C. Laabs, J. Alloys Compd. 312 (2000) 41.
[41] J.H. Zhu, P.K. Liaw, C.T. Liu, Mater. Sci. Eng. A239–A240 (1997) 260.

[42] J. Nei, K. Young, N. Simon, S. Sally (unpublished).
[43] W.J. Boettinger, D.E. Newbury, K. Wang, L.A. Bendersky, C. Chiu, U.R. Kattner, K. Young, B. Chao, Metall. Mater. Trans. A 41 (2010) 2033.
[44] L.A. Bendersky, K. Wang, W.J. Boettinger, D.E. Newbury, K. Young, B. Chao, Metall. Mater. Trans. A 41 (2010) 1891.
[45] K. Young, J. Nei, T. Ouchi, M.A. Fetcenko, J. Alloys Compd. 509 (2011) 2277.
[46] J.Y. Yu, Y.Q. Lei, C.P. Chen, J. Wu, Q.D. Wang, J. Alloys Compd. 231 (1995) 578.
[47] D. Sun, M. Latroche, A. Percheron-Guégan, J. Alloys Compd. 248 (1997) 215.
[48] M. Bououdina, H. Enoki, E. Akiba, J. Alloys Compd. 281 (1998) 290.
[49] Q.A. Zhang, Y.Q. Lei, X.G. Yang, K. Ren, Q.D. Wang, J. Alloys Compd. 292 (1999) 236.
[50] L. Chen, F. Wu, M. Tong, D.M. Chen, R.B. Long, Z.Q. Shang, H. Liu, W.S. Sun, K. Yang, L.B. Wang, Y.Y. Li, J. Alloys Compd. 293–295 (1999) 508.
[51] K.Y. Shu, X.G. Yang, S.K. Zhang, G.L. Lü, Y.Q. Lei, Q.D. Wang, J. Alloys Compd. 306 (2000) 122.
[52] Y.L. Du, X.G. Yang, Q.A. Zhang, Y.Q. Lei, M.S. Zhang, Int. J. Hydrogen Energy 26 (2001) 333.
[53] Y.H. Zhang, P. Li, X.L. Wang, Y.F. Lin, X.H. Qu, J. Alloys Compd. 364 (2004) 289.
[54] A. Visintin, H.A. Peretti, F. Ruiz, H.L. Corso, W.E. Triaca, J. Alloys Compd. 428 (2007) 244.
[55] K. Young, T. Ouchi, M.A. Fetcenko, J. Alloys Compd. 480 (2009) 428.
[56] K. Young, T. Ouchi, W. Mays, B. Reichman, M.A. Fetcenko, J. Alloys Compd. 480 (2009) 434.
[57] K. Young, T. Ouchi, M.A. Fetcenko, J. Alloys Compd. 480 (2009) 440.
[58] H.P. Klug, L.E. Alexander, X-Ray Diffraction Procedures for Polycrystalline and Amorphous Materials, second ed., John Wiley & Sons, New York, 1974, p. 656.
[59] L. Schlapbach, A. Züttle, Nature 414 (2001) 353.
[60] C. Iwakura, W.K. Choi, S. Zhang, H. Inoue, Electrochim. Acta 44 (1998) 1677.
[61] A. Zuttel, F. Meli, L. Schlapbach, J. Alloys Compd. 231 (1995) 645.
[62] K. Young, T. Ouchi, A. Banik, J. Koch, M.A. Fetcenko, Int. J. Hydrogen Energy 36 (2011) 3547.
[63] K. Young, T. Ouchi, B. Huang, M.A. Fetcenko, J. Alloys Compd., submitted for publication.